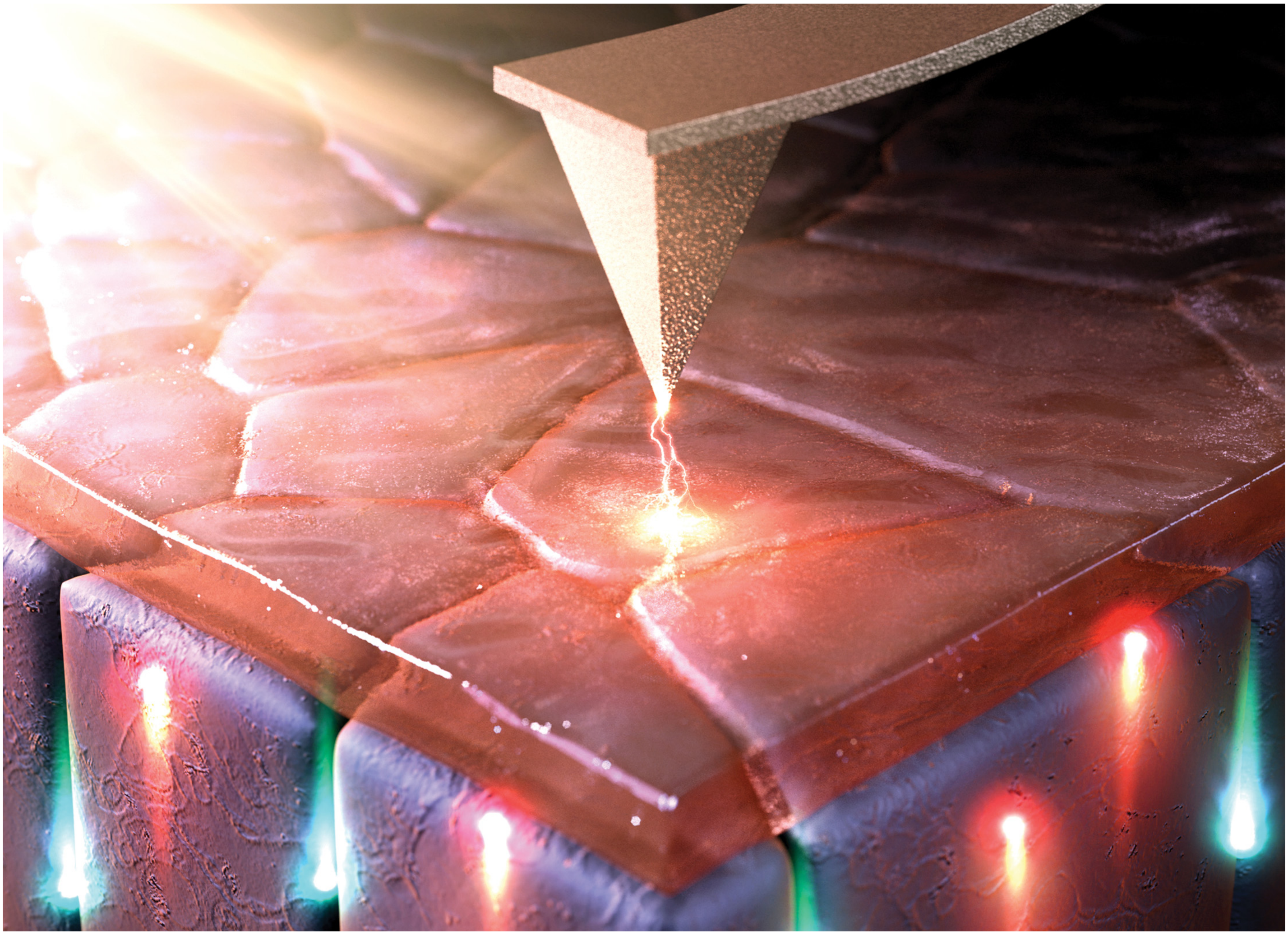

Showcasing research from Dr Yun's Nanoscale Photovoltaics Laboratory, School of Photovoltaic and Renewable Energy Engineering, UNSW Sydney, Kensington, Australia.

Efficient charge separation at localized 2D ferroelectric domains in perovskite solar cells

This work reveals the potential of ferroelectric-assisted charge separation in 2D perovskites in conjunction with conventional p–n junction photovoltaics. We fabricate high-quality perovskite devices in which a ferroelectric 2D perovskite layer with oppositely polarized regions is locally formed on top of a 3D perovskite layer. This configuration promotes distinct potential offsets between the two regions and acts as an excellent electron–hole pair separator. Our findings offer promising opportunities for the design of ferroelectric and p–n junction hybrid photovoltaic devices.

Image reproduced by permission of Jae Sung Yun from *Energy Environ. Sci.*, 2025, **18**, 5287.

As featured in:

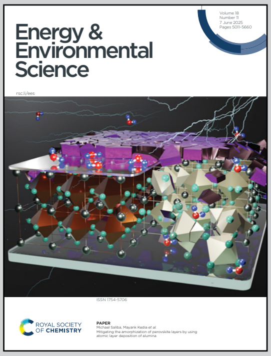

See Dohyung Kim, Jun Hong Noh, Jae Sung Yun *et al.*, *Energy Environ. Sci.*, 2025, **18**, 5287.

ROYAL SOCIETY OF CHEMISTRY

rsc.li/ees

Energy &
Environmental
Science

ROYAL SOCIETY
OF CHEMISTRY

PAPER

View Article Online
View Journal | View Issue

Check for updates

Cite this: *Energy Environ. Sci.*, 2025, **18**, 5287

Efficient charge separation at localized 2D ferroelectric domains in perovskite solar cells†

Jihoo Lim,‡[a] Seungmin Lee,‡[b] Hongjae Shim,‡[a] Lei Wang,[c] Hyeonah Cho,[b] Jincheol Kim,[d] Claudio Cazorla,[e] Yong-Jin Kim,[f] Hanul Min,[g] Minwoo Lee,[a] Xiaojing Hao,[a] S. Ravi P. Silva,[h] Jan Seidel,[c] Dohyung Kim,*[ij] Jun Hong Noh*[bg] and Jae Sung Yun*[ah]

Received 4th February 2025,
Accepted 14th April 2025

DOI: 10.1039/d5ee00640f

rsc.li/ees

Ferroelectric properties can be utilized for efficient charge carrier separation through spontaneous electric polarization. Here, we reveal the potential of ferroelectric-assisted charge separation in 2D perovskites in conjunction with conventional p–n junction photovoltaics. We fabricate high-quality perovskite devices in which a ferroelectric 2D perovskite layer with oppositely polarized regions is locally formed on top of a 3D perovskite layer. Such distinct regions are created near the grain boundary and grain interior regions within the perovskites, and their polarity can be manipulated under bias voltage and light illumination. This configuration promotes distinct potential offsets between the two regions and acts as an excellent electron–hole pair separator. Our findings offer promising opportunities for the design of ferroelectric and p–n junction hybrid photovoltaic devices, resulting in a power conversion efficiency of 26.0%, with an independently certified efficiency of 25.2%.

Broader context

Perovskite solar cells (PSCs) have emerged as a leading photovoltaic (PV) technology, but further efficiency gains require improved charge separation strategies. While conventional PSCs rely on p–n junctions, ferroelectric materials offer an alternative approach by generating internal electric fields that drive charge carrier separation. This work integrates a ferroelectric 2D perovskite with a 3D perovskite, using a solid-state in-plane growth (SIG) method. This enables precise control over localized ferroelectric polarization at grain boundaries and grain interiors, enhancing charge separation and boosting efficiency. Our devices achieve a power conversion efficiency (PCE) of 26.0% (certified at 25.2%), demonstrating the impact of ferroelectricity in hybrid perovskites. Beyond photovoltaics, this approach could benefit a wide range of optoelectronic applications, including light-emitting diodes and memory devices. By leveraging ferroelectric effects in perovskites, this study provides a new avenue for designing more efficient and stable perovskite devices.

Introduction

Perovskite solar cells (PSCs) consist of an active perovskite absorber positioned between multiple layers of charge-selective materials, facilitating unidirectional current flow and have achieved excellent power conversion efficiencies (PCEs).[1–3] The conventional approach to constructing high-efficiency solar cells involves charge separation and collection through p–n junctions or p–i–n structures. In halide PSCs, a p–n junction is established between the interface of perovskites

---

[a] *Australian Centre for Advanced Photovoltaics (ACAP), School of Photovoltaic and Renewable Energy Engineering, University of New South Wales, Sydney, NSW 2052, Australia*
[b] *School of Civil, Environmental and Architectural Engineering, Korea University, Seoul 02841, Republic of Korea. E-mail: junhnoh@korea.ac.kr*
[c] *School of Materials Science and Engineering, University of New South Wales, Sydney, NSW 2052, Australia*
[d] *Sustainable Energy Research Centre, School of Engineering, Macquarie University, Sydney, NSW 2109, Australia*
[e] *Departament de Física, Universitat Politècnica de Catalunya, Campus Nord B4–B5, Barcelona 08034, Spain*
[f] *Photovoltaics Research Department, Korea Institute of Energy Research, Daejeon 34129, Republic of Korea*
[g] *Department of Integrative Energy Engineering & KU-KIST Graduate School of Converging Science and Technology, Korea University, Seoul 02841, Republic of Korea*
[h] *Department of Electrical and Electronic Engineering, Advanced Technology Institute (ATI), University of Surrey, Guildford GU2 7XH, UK. E-mail: j.yun@surrey.ac.uk*
[i] *Department of Advanced Materials Engineering, Chungbuk National University, Cheongju 28644, Republic of Korea. E-mail: dohyungkim@chungbuk.ac.kr*
[j] *Department of Urban, Energy, and Environmental Engineering, Chungbuk National University, Cheongju 28644, Republic of Korea*

† Electronic supplementary information (ESI) available. See DOI: https://doi.org/10.1039/d5ee00640f

‡ J. L., S. L., and H. S. contributed equally to this work.

and charge transporting layers,[4,5] and the difference in charge carrier affinity facilitates free charge separation and charge transport.[6,7] Various routes for efficient charge separation, such as defect engineering in which deep trap defects are well-passivated, have been demonstrated.[8–10]

As an alternative for charge separation, ferroelectric photovoltaics (PVs), such as $BiFeO_3$, operate on principles entirely distinct from solar cells based on conventional p–n junctions, yet their device efficiency remains relatively poor.[11–14] They have been demonstrated to achieve successful polarization-assisted charge separation by creating a substantial electrostatic potential difference between different polarization orientations. Notably, at the domain walls of ferroelectric thin films, abrupt changes in polarization orientation can occur, resulting in the creation of a strong electrostatic potential difference. This potential difference can facilitate the separation of charge carriers by pushing electrons and holes in opposite directions along the electric fields. Therefore, the domain walls can serve as effective charge separation interfaces. When this feature is coupled with the nanoscale structure within the excitonic diffusion lengths, enhanced PV devices can be accessed by this design.

Recently, the ferroelectric nature of some of 2D halide perovskites has been found to facilitate strong polarization, making them promising candidates for exploiting ferroelectric properties in charge separation for solar cells.[15–17] However, several challenges are associated with using 2D perovskites alone, due to their short carrier diffusion length compared to their 3D counterparts and their large bandgap that limits the absorption of solar radiation, and leads to reduced efficiency.[18] A common approach has been to deposit a thin layer of 2D perovskites on top of a 3D perovskite absorber to passivate surface defects and create a built-in electric field due to energy level differences, resulting in enhanced charge separation and collection.[19–21] Recently, ferroelectric 2D perovskites have been integrated with 3D perovskites, reducing recombination at the 2D/3D interface through ferroelectric polarization. This highlights the potential of ferroelectric polarization for further enhancing device performance.[22] However, challenges remain in precisely controlling the thickness of the 2D ferroelectric layer and locally manipulating its polarization. This issue arises from the difficulty in achieving precise control over the composition and formation of high quality 2D perovskites due to the conventional method of coating 2D perovskites based on organic amine salt onto the 3D perovskite films, followed by the inter-reaction between them.[23–25] It has recently been reported that the solid-state in-plane growth (SIG) method enables the formation of intact 2D/3D junctions with a pristine 2D single phase perovskite on top of the 3D perovskite film, allowing for the realization of high quality 2D perovskites.[26] However, the ferroelectric properties of the resulting 2D perovskites have not yet been fully developed.

In this work, we demonstrate ferroelectric polarization-driven enhanced charge separation using highly crystalline 2D phenylethylammonium lead halide (PEA_2PbI_4) perovskites. Even though PEA_2PbI_4 perovskite is known to be a non-ferroelectric material,[27] we show that it exhibits ferroelectric characteristics after SIG processing with an underlying methylammonium (MA)-containing 3D perovskite, consistent with previously reported ferroelectric nature of 2D PEA-MA Ruddlesden–Popper (RP) perovskites.[28] As a result, a 2D MA^+-reacted PEA_2PbI_4 perovskite layer was successfully formed on top of the 3D $(FAPbI_3)_{0.95}(MAPbBr_3)_{0.05}$ perovskite absorber layer *via* the SIG method. Based on light- and bias-dependent piezoresponse force microscopy (PFM) and Kelvin probe force microscopy (KPFM) measurements, we demonstrate that the electronic and polarization properties of the 2D perovskite are altered at the grain boundary (GB) and grain interior (GI) regions under electrical bias and illumination. Our *ab initio* density functional theory (DFT) calculations reveal that local epitaxial strain induces polarization vectors in opposite directions, depending on whether the strain is compressive or tensile. Consequently, the strain difference between GB and GI regions creates a unique electronic architecture that facilitates effective charge carrier separation at the surface, leading to a PCE of 26.0% (independently certified at 25.2%).

To exploit ferroelectric characteristics in PSCs, we deposited a 2D PEA_2PbI_4 layer on top of a 3D formamidinium lead iodide ($FAPbI_3$) containing 5% of methylammonium lead bromide ($MAPbBr_3$) perovskite layer using the SIG process by applying adequate heat and pressure, which controls the thickness of the 2D PEA_2PbI_4 layer. We selected two different pressures for forming the 2D perovskite layer, namely SIG-LPR (low pressure – 0.65 kPa) and SIG-HPR (high pressure – 25 MPa), respectively. Fig. 1(a) and (b) display the cross-sectional scanning electron microscopy (SEM) images of the control and SIG-HPR perovskite films, respectively. From Fig. 1(c) and Fig. S1 (ESI†), the control and SIG-LPR perovskite films exhibit similar surface morphologies, whereas the SIG-HPR film shown in Fig. 1(d) displays corrugated features within the grains. However, the surface roughness is reduced after reacting with 2D perovskites, as shown in Fig. S2 (ESI†), with the SIG-HPR film exhibiting the lowest roughness value among all samples. Consequently, we postulate that the SIG-LPR film was deposited with a non-uniform layer of the 2D PEA_2PbI_4 perovskite, in contrast to the uniform layer in the SIG-HPR film. Each corrugated grain in the SIG-HPR film may stem from terraced topographic features at the microscale in 2D perovskites,[29,30] attributed to the uniform and well-controlled deposition of 2D perovskites on top of 3D perovskites,[31] through the SIG process. Typically, these steps occur naturally on the surface of a crystal due to the specific arrangement of atoms within the lattice structure. In addition, we performed X-ray diffraction (XRD) measurements on the pure 2D PEA_2PbI_4 film, the control, and the SIG-HPR films, as represented in Fig. 1(e). The SIG-HPR film exhibits the (002) peak of 2D PEA_2PbI_4 (at approximately 5.4°),[32] without unwanted non-perovskite or mixed quasi 2D phases. Also, the peak of PbI_2 disappears for the SIG-HPR film compared to that of the control and SIG-LPR film, as shown in Fig. S3 (ESI†). The SIG-LPR film exhibits no (002) peak, likely due to the signal being beyond the XRD detection limit and possibly attributed to not fully optimized formation of the 2D PEA_2PbI_4 perovskite. The pure 2D PEA_2PbI_4 film peak has a full width at half-

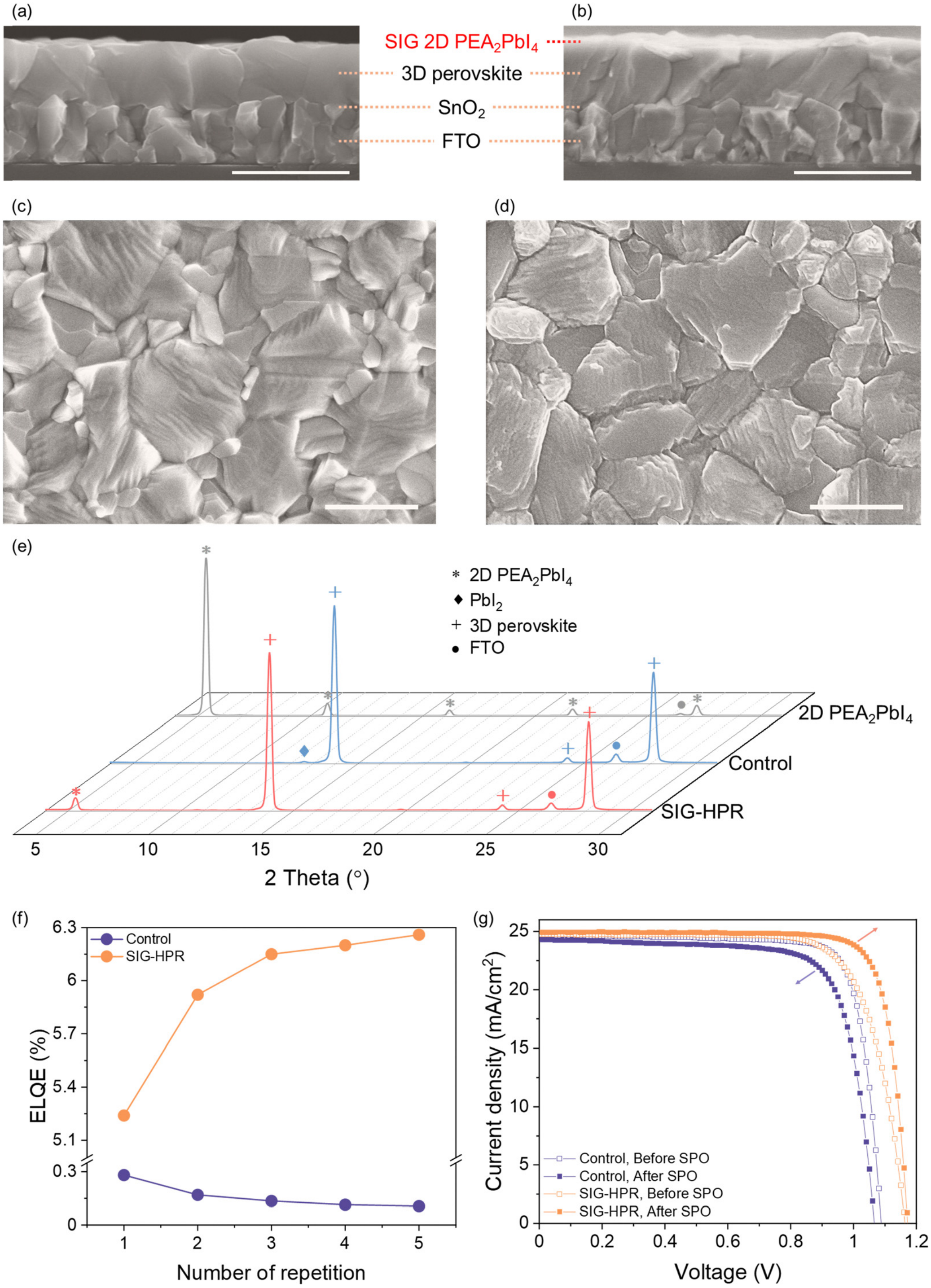

Fig. 1 Cross-sectional SEM images of (a) control, and (b) SIG-HPR perovskite films, top-view SEM images of (c) control, and (d) SIG-HPR perovskite films, (e) XRD 2-theta patterns of control (3D perovskite only), a pure 2D perovskite film (n = 1, PEA_2PbI_4), and SIG-HPR perovskite films, (f) ELQE measurement, and (g) J–V performance before and after SPO measurements of control and SIG-HPR perovskite devices. The scale bar represents 1 μm.

maximum (FWHM) of 0.176° and SIG-processed PEA_2PbI_4 on top of the SIG-HPR film shows a similar value of 0.194°, indicating the formation of a highly crystalline pure 2D perovskite layer on top of the 3D perovskite layer. However, grazing incidence X-ray diffraction (GIXRD) measurement using an incident angle of 0.5° (penetration depth of ∼70 nm),[33] presented in Fig. S4 (ESI†), shows that the SIG-LPR film exhibits only a small peak at around 5.4°. To precisely distinguish, we performed GIXRD measurement on the SIG-LPR film again using a lower incident angle of 0.2° (penetration depth of ∼25 nm),[34] focusing on the surface region, as shown in Fig. S5 (ESI†). This measurement reveals that the SIG-LPR film exhibits a weak 2D PEA_2PbI_4 perovskite peak. These results are consistent with our SEM results for the SIG-LPR film presented in Fig. S1 (ESI†), which display a comparable surface morphology to the control film. Photoluminescence (PL) measurements, shown in Fig. S6 (ESI†), further confirm the formation of the PEA_2PbI_4 ($n = 1$) phase[35] at approximately 520 nm in the SIG-HPR film, while this peak was absent in the control perovskite film. Therefore, we conclude that only the SIG-HPR film demonstrates a high-quality 2D perovskite structure.

To investigate the effect induced from the homogeneous formation of the 2D PEA_2PbI_4 perovskite on top of the 3D perovskite on device performance, we fabricated devices using the control and SIG-HPR films. As shown in Fig. S7 (ESI†), we measured the electroluminescence quantum efficiency (ELQE) of each device operating under dark conditions, in accordance with the current density. The SIG-HPR device displayed higher ELQE values compared to the control device at the corresponding values of J_{SC}. Fig. 1(f) represents ELQE measurements used to evaluate the recombination behavior of the control and SIG-HPR devices, by operating the solar cells as light-emitting diodes. Notably, only the SIG-HPR device showed unique behavior in ELQE as the measurements were repeated. The control device initially exhibited an ELQE of 0.28%, which decreased to 0.1% after five repetitions. In contrast, the ELQE of the SIG-HPR device increased from an initial 5.24% to a final 6.26%. This trend is consistent with the increase in steady-state power output (SPO), which involves applying a bias under continuous illumination and was observed only in the SIG-HPR device (see Fig. S8, ESI†).

We then compared the *J–V* curves of the control and SIG-HPR devices before and after SPO measurements, as shown in Fig. 1(g). The improvement in the performance was observed only in the SIG-HPR device, which is consistent with the increased SPO. The initial *J–V* curves and parameters for the control and SIG-HPR films after careful optimization are provided in Fig. S9 (ESI†). As shown in Fig. S8 (ESI†), the SPO values were approximately 20.5%, and 22.4% for the control and SIG-HPR devices, respectively. However, a gradual increase in SPO was observed only for the SIG-HPR device. The *J–V* curves after applying bias under illumination and the corresponding results are summarized in Fig. S10 (ESI†). After applying illumination and bias, the SIG-HPR device exhibited the best performance with a PCE of 24.1% with negligible hysteresis, while the control device showed a reduced PCE of 20.1%.

To examine the role of the 2D PEA_2PbI_4 perovskite layer, we performed piezoresponse force microscopy (PFM) to study the microstructure and local polar properties. Fig. 2(a) illustrates the PFM measurement setup for the SIG-HPR film, in which the 2D PEA_2PbI_4 is deposited on top of the 3D perovskite, and a SnO_2 layer is used as the electron transport layer (ETL), deposited onto an FTO-coated glass substrate. PFM measurements were conducted under dark conditions to eliminate excess charge carrier effects.[36] The PFM amplitude maps of the control and SIG-HPR films are shown in Fig. 2(b) and (c), respectively. In the control film, no discernible electromechanical response is observed, as shown in Fig. 2(b), with only noise-level amplitude signals detected. This is understandable, as 3D FA-based perovskites typically do not exhibit ferroelectric properties due to the rigid states of the FA molecule.[37] In conventional oxide materials, directly probing the ferroelectricity in ultra-thin films is often difficult and usually limited by large leakage currents.[38] On the other hand, the SIG-HPR film exhibits a strong amplitude response with pronounced contrast emerging near the GB regions compared to the GI regions, as shown in Fig. 2(c). We suspect that the GB regions in the underlying 3D perovskite have different local chemistry, lattice strain, and atomic structure compared to the GI regions.[37,39–41]

We then further investigated the potential existence of ferroelectric polarization in SIG-processed 2D PEA_2PbI_4 perovskite films. As shown in Fig. S11 (ESI†), the pure 2D PEA_2PbI_4 perovskite film without MA exhibits non-ferroelectric behavior, which is consistent with the previously reported literature.[27] Interestingly, however, the SIG-processed 2D PEA_2PbI_4 layer on top of $FAPbI_3$ with 5% of $MAPbBr_3$ perovskite resulted in ferroelectric characteristics as represented in Fig. S12 (ESI†). To identify the origin of this ferroelectric behavior, we examined SIG-processed 2D PEA_2PbI_4 combined with the pure 3D $FAPbI_3$ perovskite (without any MA incorporation), which demonstrated non-ferroelectric properties, as shown in Fig. S13 (ESI†). Consequently, we propose that the ferroelectric characteristics arise from the incorporation of MA in the $FAPbI_3$ layer, similar to previously reported MA-based RP PEA perovskites, where ion translation plays a role.[28] A comprehensive discussion of the ferroelectric properties exhibited by the MA^+-incorporated 2D PEA_2PbI_4 perovskite (referred to as SIG-HPR 2D $(MA)PEA_2PbI_4$), along with the potential influence of ionic motion can be found in the Supplementary Text in the ESI.† The SIG-HPR 2D $(MA)PEA_2PbI_4$ belongs to the RP perovskite family. Previous research[28] has confirmed its non-centrosymmetric nature through second harmonic generation (SHG) studies. Furthermore, our XRD results, shown in Fig. 1(e), reveal the presence of distinct (002) diffraction peaks of 2D PEA_2PbI_4, suggesting that the (002) planes are aligned parallel to each other and stacked along the *c*-axis, forming a layered perovskite with an orthorhombic crystal structure.

Considering that the SIG-HPR 2D $(MA)PEA_2PbI_4$ film exhibits the highest out-of-plane piezo-response, the spontaneous polarization, *e.g.* unit-cell deformation, is likely oriented normal to the surface.[42] As shown in Fig. 2(d) and (e), spectroscopic PFM measurements of the SIG-HPR 2D $(MA)PEA_2PbI_4$ film were performed under dark conditions. For the SIG-LPR film, non-hysteretic PFM curves indicate absent or unstable ferroelectricity, as displayed in Fig. S14 (ESI†). In contrast, the SIG-HPR film reveals ferroelectric-like behavior, such as butterfly-shaped amplitude and hysteretic phase loops as a function of applied bias voltage.[43] This phenomenon results from well-established ferroelectric properties of 2D perovskites.[44–47] We further explored whether external stimuli, such as electrical bias and illumination can modulate polarization states under operating conditions relevant to solar cells. Illumination plays multiple roles in perovskites. Our previous study[42] demonstrated that it induces structural deformation, which is fundamentally linked to photo-induced lattice expansion.[48] This light-induced effect alters the internal electric polarization, often leading to

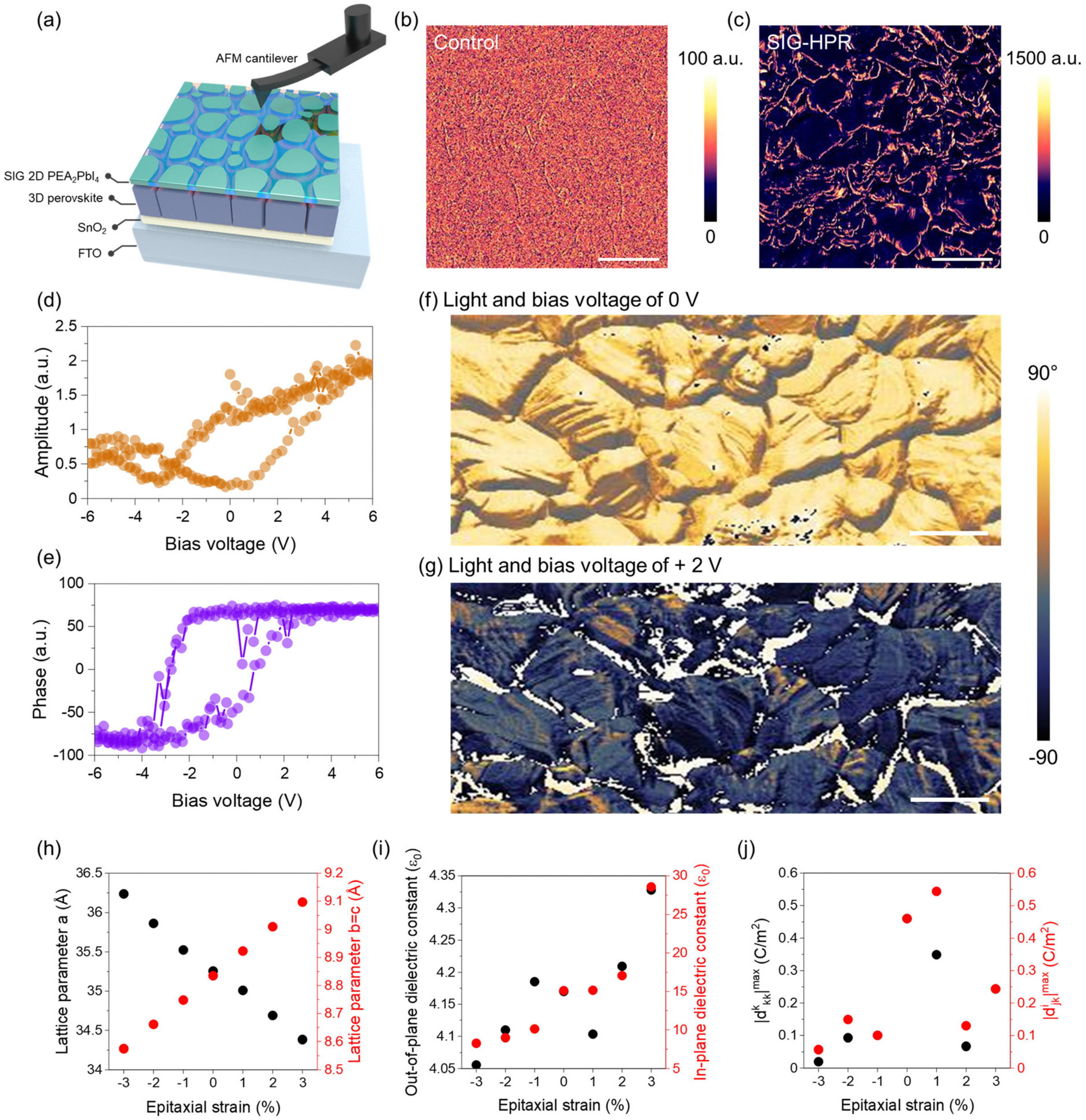

Fig. 2 (a) Schematic illustration of PFM measurement, PFM amplitude maps of (b) control and (c) SIG-HPR perovskite films, (d) PFM amplitude, (e) PFM phase-switching spectroscopy loops, demonstrating ferroelectric-like butterfly amplitude and hysteretic phase loops on the SIG-HPR film surface, PFM phase spatial maps under illumination with applied bias voltages of (f) 0 V, and (g) +2 V, respectively. DFT results of the epitaxial strain dependence of (h) lattice parameters, (i) dielectric constant, and (j) piezoelectric coefficient. The scale bar represents 1 μm.

structural changes and variations in optical properties. Fig. 2(f) and (g) show a PFM phase spatial map under illumination with applied bias voltages of 0 V and +2 V. We applied a bias voltage of +2 V for switching the polarity, as this corresponds to the switching voltage in the SIG-HPR 2D (MA)PEA_2PbI_4 film, as clarified by the PFM hysteresis loop shown in Fig. 2(e). Notably, the combination of electrical bias and illumination leads to substantial changes in piezoresponse at both GB and GI regions. The evolution of phase responses as a function of bias at five different points across the GB and GI domains was observed from the PFM phase maps, and the obtained curves are in flipped directions, as presented in Fig. S15 (ESI†). Note that illumination generates charge carriers that separate under an external electric field inducing polarization[49] and causes structural variations,[42] thereby impacting the orientation of dipoles[50] and consequently lead to the material's polarization. These effects can vary depending on various factors such as chemical composition, crystal structure, and crystallinity. Further investigation reveals that GBs can be more effectively polarized than GIs (see Fig. S16 and S17, ESI†), consistent with the observed PFM images shown in Fig. 2(f) and (g). In ferroelectric materials, polarization directions are typically oriented in two opposite directions, conventionally labelled as +P and −P.[51] The associated charge density forms electric dipoles, which can create unique electric fields near the GB and GI regions. The SIG-HPR 2D (MA)PEA_2PbI_4 film exhibits the PFM phase shift of approximately 85° (close to 90°) and 123° (over 90°) at the GB and GI regions (from bias voltage of 0 V to +2 V), respectively. A phase difference of 180° is typically observed in PFM measurements when polarization directions are completely reversed. In many cases, the polarization states are displayed as +90° and −90°, depending on how the phase offset or reference is defined during signal processing. Although this appears as a ±90° phase change, it actually corresponds to a 180° phase difference, indicating polarization reversal (see the Supplementary Text in the ESI†). In addition, the higher signal of out-of-plane PFM amplitude compared to that of in-plane signal, as shown in Fig. S18 (ESI†), suggests that the sample exhibits a more dominant out-of-plane signal, indicating that the net charge polarization is oriented in a vertical direction. To accurately analyse the phase shifts induced by light and bias conditions, as shown in Fig. 2(f) and (g), we measured the first and second harmonic responses in PFM, as presented in Fig. S19 (ESI†). The first harmonic response indicates ferroelectric behavior, while the second harmonic response reflects ion migration.[52–54] A linear increase in the first harmonic response, without a change in the second harmonic, suggests that ionic motion is excluded, supporting the evidence of ferroelectricity. Consequently, it is expected that opposite electric polarization vectors are formed between GB and GI regions in a vertical direction as depicted in Fig. S20 (ESI†). Although the Curie temperature of the $n = 1$ phase has not been explicitly reported, temperature-dependent SHG studies on RP halide perovskites with $n = 2$–4 reveal a gradual decrease in the SHG signal within the 140–180 °C range, indicating a transition from the ferroelectric to paraelectric phase. Notably, the $n = 5$ composition exhibits a Curie temperature of 171–176 °C.[28] These findings suggest that polarization in this material family remains stable well above room temperature, underscoring the significance of the observed ferroelectric behavior and its potential for practical applications. Furthermore, we performed DFT simulations to study the epitaxial strain dependence of lattice parameters and dielectric constants, and piezoelectric coefficients, as shown in Fig. 2(h)–(j). As it is commonly done,[55,56] epitaxial strain (η) was reproduced by fixing the length and angle of the two in-plane lattice vectors, namely $b = c$ and $bc = 90$ degrees, and fully optimizing the out-of-plane lattice vector, a. The epitaxial strain was then defined as $\eta = (b/b_0 - 1) \times 100$, where b_0 corresponds to the equilibrium value of the in-plane lattice vector. All atomic positions were optimized until the maximum atomic force component was lower than 0.005 eV Å^{-1}. From these epitaxially constrained DFT simulations, we identified one non-centrosymmetric structure (triclinic, space group $P1$) that is vibrationally stable in our 2D/3D junction perovskite system, as shown in Fig. S21 (ESI†). As shown in Fig. 2(h), the structural parameters evolve under epitaxial strain as expected. Specifically, the a (or bc) lattice parameter decreases (increases) under tensile strain (positive strain) and increases (decreases) under compressive strain (negative strain). In all cases, the variation of the lattice parameters follows a nearly linear trend. Fig. 2(i) illustrates the dielectric properties of the system under epitaxial strain. Generally, both the in-plane and out-of-plane components of the dielectric tensor increase under tensile strain and decrease under compressive strain. However, the variation in the in-plane components (y–z) is significantly larger than that of the out-of-plane component, as reflected by the differences in the two y-axes in the figure. Similarly, Fig. 2(j) confirms this trend, showing that both in-plane and out-of-plane components of the piezoelectric tensor increase under tensile strain and decrease under compressive strain. The greater variation in the in-plane components compared to the out-of-plane component aligns well with our PFM measurements, which reveal two distinct and opposite piezoelectric tensor components, GBs and GIs, depending on epitaxial strain. Since GBs and GIs exhibit opposite strain responses,[57] different reactions to external electric fields can be expected in the two epitaxial strain regimes. Based on the simulation results, we observed that the out-of-plane and in-plane components change depending on the internal strain. When applying this to the GB and GI regions, we propose that the difference in strain may have influenced the phase signal. While strain does induce deformation, very small strains may not cause a change in the material's phase but rather induce lattice distortions in a similar manner. As a result, strain can affect the piezoelectric response, which is a characteristic behavior of ferroelectrics. Therefore, the polarization reversal observed in the PFM phase signal between the GBs and GIs may be attributed to the strain-induced variations between these regions.

To validate the ferroelectric behavior and visualize the local charge separation from electric dipoles formed in the 2D perovskites, we performed light- and bias-dependent KPFM measurements under illumination for control and SIG-HPR films. A schematic of our KPFM measurement under illumination is depicted in Fig. S22 (ESI†), where we employed the same sample configuration as shown in Fig. 2(a). In the current configuration, an increase in CPD directly refers to an increase in hole accumulation at the top surface, while electrons flow toward the ETL/FTO side. Under illumination, the CPD values are determined by the accumulation of excess charge carriers at the top surface of the sample.[58,59] We investigated the CPD change upon biasing the atomic force microscopy (AFM) tip under illumination with an applied bias from 0 V to +2 V to pole the 2D perovskite layer. The full series of CPD spatial maps from the light- and bias-dependent KPFM measurements, along with the corresponding CPD distribution curves, are presented in Fig. S23 (ESI†). Mean CPD curves of the control and SIG-HPR films under illumination, with and without an applied bias voltage of +2 V, are shown in Fig. 3(a) and (b). The control film exhibits a reduction in overall CPD when the bias is applied. As shown in Fig. S24 (ESI†), the SIG-LPR film also shows a decrease in CPD, but at a slower rate compared to the control film (see Fig. S23, ESI†), suggesting a partial suppression of halide ion migration, possibly due to the surface passivation effect of the 2D perovskite layer. However, the SIG-HPR film shows an increase in overall CPD values. As expected, the top 2D ferroelectric perovskite layer of the SIG-HPR film is poled due to the applied bias, which may attract

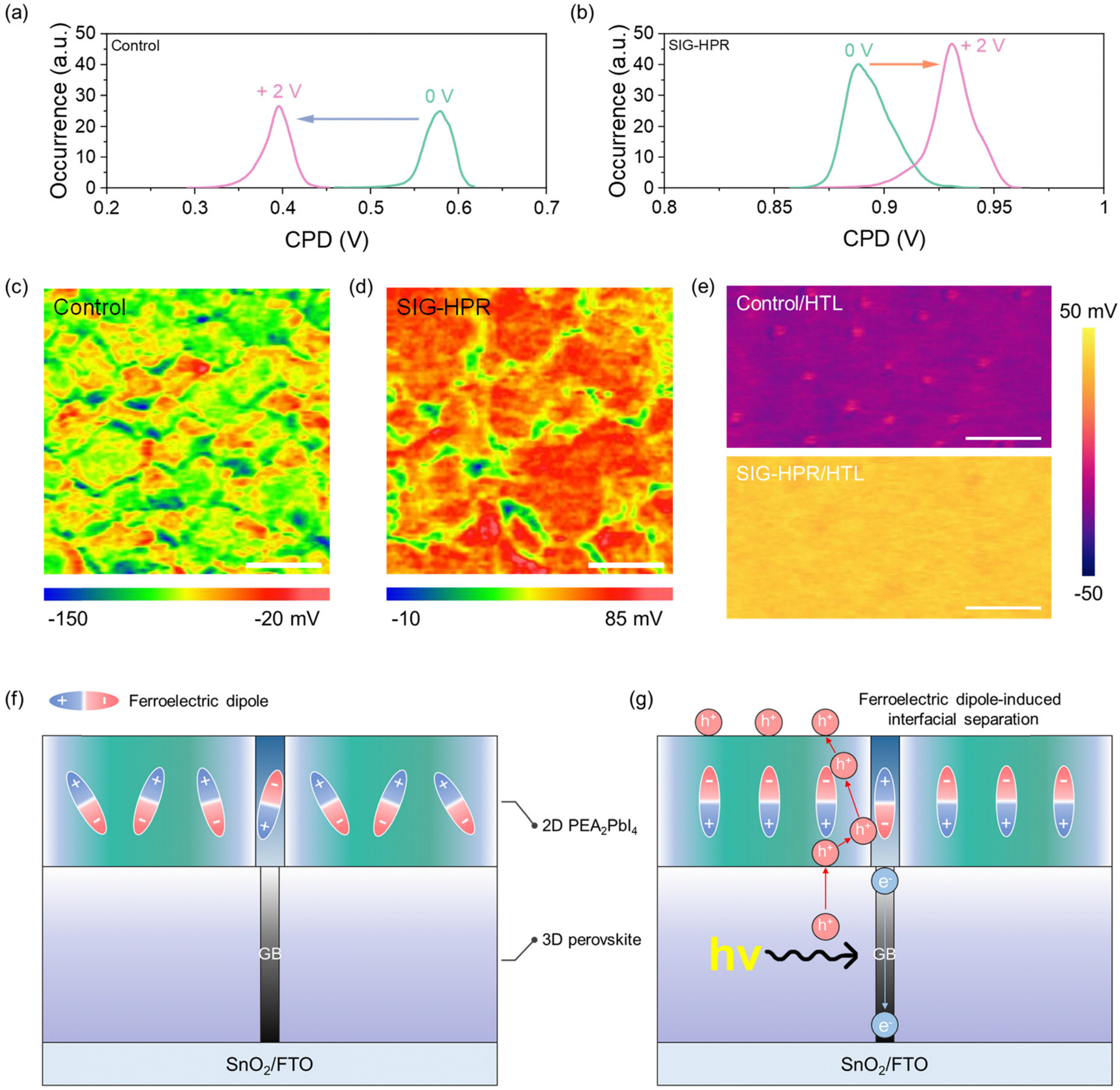

Fig. 3 Light- and bias-dependent KPFM measurements. CPD distribution curves for (a) control, and (b) SIG-HPR perovskite films with applied tip biases of 0 V and +2 V, surface photovoltage (SPV) spatial maps of (c) control, and (d) SIG-HPR perovskite films, (e) CPD spatial maps subtracted from +1 V to 0 V of control and SIG-HPR films with an HTL on top of the perovskite surface under illumination with applied tip biases of 0 V and +1 V, schematic illustrations of selective charge separation occurred by opposite dipoles formed at GB and GI regions (f) before and (g) after ferroelectric polarization induced by light illumination and biasing. Corresponding potential fluctuations formed across the GB and GI regions. The scale bar represents 1 μm.

more excess holes. To observe local CPD variation, we also plotted the average CPD values at GBs and GIs in the control film, and compared them with the values at the GB and GI regions for SIG-HPR films, with respect to the bias voltage, as shown in Fig. S25 (ESI†). The control film shows a continuous decrease in CPD under illumination as the bias voltage increases from 0 to +2 V, with the CPD variation between GBs and GIs remaining nearly unchanged. In contrast, the SIG-HPR film shows a gradual increase in overall CPD under the same conditions, along with a steady increase in the CPD change between GBs and GIs. This enhanced band bending at GBs promotes more efficient charge separation by facilitating stronger carrier separation.[59] This behavior can be attributed to the distinct polarization at GBs and GIs, which differs from that observed in the control film.

This can be further investigated by subtracting the CPD map measured at +2 V from the CPD map at 0 V for both the control and SIG-HPR films, as shown in Fig. 3(c) and (d), respectively. The subtracted CPD maps at each bias voltage are shown in Fig. S26 (ESI†). As can be seen, grain-to-grain contrast is not clear for the control film. Meanwhile, there is a distinct CPD contrast difference between GB and GI regions for the SIG-HPR film as evident from Fig. 3(c) and (d). Additionally, the CPD distribution within individual grains is relatively homogeneous in the SIG-HPR film compared to the control film under applied bias. A representative grain from each film was selected and its CPD values are shown in Fig. S27 (ESI†). The control film exhibits an inhomogeneous CPD distribution within a grain at each bias voltage, whereas the SIG-HPR film shows progressively enhanced homogeneity as the bias voltage increases.

To establish a direct correlation with device performance, we carried out illumination- and bias-dependent KPFM measurements with an HTL layer (Spiro-OMeTAD) atop control and SIG-HPR perovskite films. Due to the positive nature of the HTL, it is expected that the 2D perovskite film experiences a similar effect of applying positive bias voltages, as observed in the above measurements. The KPFM results are summarized in Fig. S28 (ESI†), and the corresponding CPD distribution curves are shown in Fig. S29 (ESI†). While the control film exhibits a variation of −0.019 V in CPD as the bias voltage increases from 0 V to +1 V, the CPD of the SIG-HPR film gradually increases, resulting in increased CPD variations of 0.039 V. This can be visualized by subtracting the CPD map measured at +1 V from the map at 0 V for both the control and SIG-HPR films with an HTL on top of the surface, as shown in Fig. 3(e). In addition, normalized CPD values in Fig. S30 (ESI†) show that the higher CPD variation in the SIG-HPR film, compared to the control film, is responsible for the improved hole extraction induced by ferroelectric polarization and the combined effects of illumination and bias. Furthermore, the FWHM of the CPD distribution curves indicates that the SIG-HPR film exhibits a more uniform distribution of surface charge resulting from ferroelectric polarization, as shown in Fig. S31 (ESI†).

Fig. 3(f) and (g) show schematics of the charge separation mechanism driven by selective ferroelectric polarization in the SIG-HPR film. Fig. 3(f) represents the state in which the electric dipoles exist without external bias and light, and they are disordered, resulting in low spontaneous polarization. However, with applying bias under illumination, as shown in Fig. 3(g), the alignment of electric dipoles improves, contributing to the enhancement of local ferroelectric polarization. For charge carriers that are separated near the surface of the 3D perovskite layer, holes are repelled by the positive dipole at the bottom of the grains and attracted by the negative dipole beneath the GB region. They then move through the grains toward the surface due to the negative dipole at the top of the grains. Additionally, due to the positive dipole formed at the bottom of the grains in the 2D perovskite layer, electrons that have migrated cannot travel upward because of the negative dipole at the top of the grains. Instead, they move toward the GB region and then descend to the bottom *via* the negative dipole formed at the bottom of the GB region. Therefore, selective charge separation can occur between GB and GI regions, due to the existence of oppositely oriented dipoles formed in these domains. Our KPFM results on the SIG-HPR film show a relatively lower CPD at the GB region compared to the GI region upon positive biasing (see Fig. S25, ESI†). The lower potential at GB regions implies electron accumulation, while the higher potential at GI regions promotes hole accumulation. A type-II band alignment is required for allowing the extraction of holes and blocks the other type as shown in UPS measurement in Fig. S32 (ESI†). Fundamentally, carrier separation occurs at the 2D/3D interface rather than within the 2D PEA_2PbI_4 perovskite layer. Based on our results, we propose that the combined effects of type-II band bending and ferroelectric domain engineering, induced by ferroelectric 2D PEA_2PbI_4, create regions with distinct polarization directions. These domains serve as potential wells and barriers, further aiding in the spatial separation of charge carriers. Electrons tend to migrate toward positively polarized regions, while holes migrate toward negatively polarized regions (GBs and GIs in Fig. 2(g), respectively).

The enhanced charge separation induced by ferroelectric polarization can be further clarified by performing time-resolved photoluminescence (TRPL) measurements, from which differential lifetimes were calculated to distinguish between charge extraction and trap-assisted recombination, as depicted in Fig. 4(a). The SIG-HPR film exhibited a longer average lifetime compared to the control film, indicating reduced nonradiative losses in the SIG-HPR film. In Fig. 4(b), the differential TRPL decay curves show a significantly steeper initial transition within the first 30 ns and a prolonged lifetime beyond 100 ns for the SIG-HPR film, compared to the control film, suggesting more efficient hole extraction at the 2D PEA_2PbI_4/3D perovskite interface. The best-performing SIG-HPR perovskite device, containing 35% MACl, achieves an SPO of 25.3% (see Fig. 4(c)) and an impressive certified PCE of 25.2% (see Fig. 4(d)), with negligible hysteresis. The statistical data of device performance are provided in Fig. S33 (ESI†). As expected, the SIG-LPR device demonstrated better performance than the control device, attributed to the surface passivation effect of the 2D perovskite layers. Notably, there was no significant difference in J_{SC} values among the three devices, which were comparable to previously reported J_{SC} values of highly efficient PSCs (see Table S1, ESI†). However, the SIG-HPR device exhibited the highest FF and V_{OC}, indicating that ferroelectric dipoles are well-aligned due to the distinct polarization at GBs and GIs, in contrast to the control and SIG-LPR devices. This outstanding performance is attributed to enhanced charge separation and collection driven by ferroelectric polarization, induced by the uniform formation of 2D perovskites. This is reflected in the enhanced external quantum efficiency (EQE) of the SIG-HPR device across both the short-wavelength (350–450 nm) and long-wavelength (750–850 nm) regions, as shown in Fig. S34 (ESI†). This improvement suggests that the uniform deposition of the 2D perovskite layer in the SIG-HPR device enhances charge transport efficiency. Although there is a small hysteresis in the SIG-HPR device, it is evident that the polarization between the GBs and GIs remains nearly unchanged when bias voltages from +1 to +2 V are applied, as depicted in Fig. S35 (ESI†). This indicates that once polarization is initiated, it will be maintained within the positive bias voltages. Since both the forward and reverse bias voltages are swept within the positive bias voltage range, no substantial changes in the polarization states are expected.

This enhanced device performance is independently certified with an efficiency of 25.2% as shown in Fig. S36 (ESI†). Additionally, the operational stability of the encapsulated devices was assessed using maximum power point tracking (MPPT) under continuous 1-sun-equivalent white-light LED

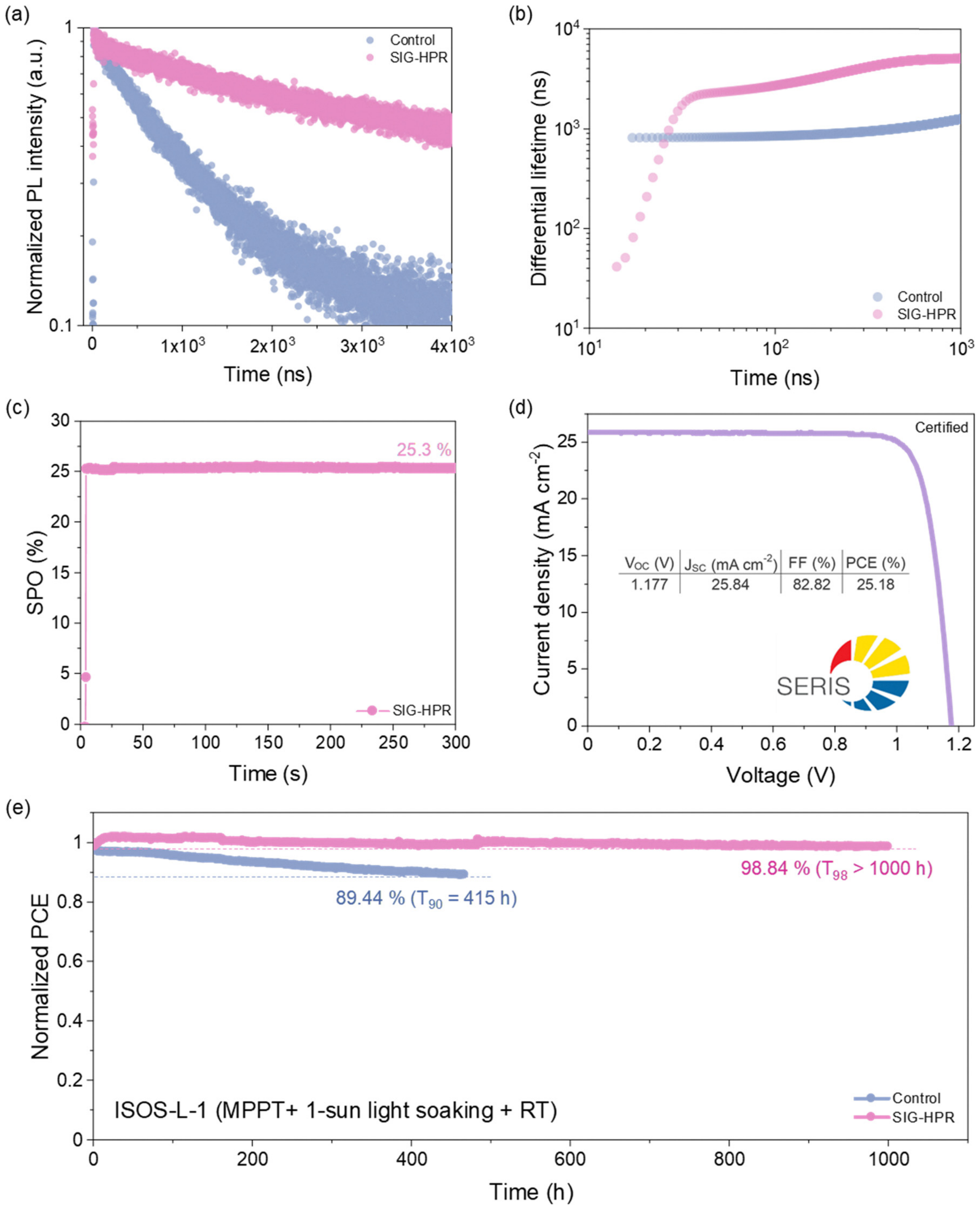

Fig. 4 Ferroelectric polarization-assisted device performance. (a) TRPL measurement, (b) computed differential lifetimes, (c) steady-state power output (SPO), measured for 300 s at a fixed voltage near the maximum power point (MPP) identified in the *J*–*V* curves, (d) *J*–*V* curve of the certified SIG-HPR device and the inset shows the corresponding *J*–*V* parameters, and (e) operational stability test of the control and SIG-HPR perovskite devices under 1-sun illumination at room temperature.

illumination, as represented in Fig. 4(e). The SIG-HPR device maintained approximately 98.8% of its initial PCE over 1000 hours, while the control device retained only 89.4% of its initial PCE after 415 hours. The SIG-HPR device may exhibit a better balance between electron and hole injection, leading to improved radiative recombination and resulting in better stability compared to the control device. This indicates that the SIG-HPR device not only achieved high efficiency but also demonstrated excellent operational stability. These results highlight that integrating ferroelectric 2D perovskite engineering, specifically using 2D PEA_2PbI_4, is a promising strategy to significantly enhance both the efficiency and stability of PSCs.

Conclusion

We demonstrate the potential of ferroelectric polarization-enhanced charge separation in improving the performance of conventional p–n junction PSCs. Our study utilized highly crystalline 2D PEA_2PbI_4 perovskites and showed that selective polarization occurs between the grain boundary and interior regions. We further reveal that, under electrical bias and illumination, ferroelectric polarization can be tuned, forming opposite dipoles at these regions, resulting in efficient charge separation. Importantly, our findings show that the use of ferroelectric polarization in PSCs led to a remarkable power conversion efficiency of 26.0% (with a certified efficiency of 25.2%). Our work highlights the potential of ferroelectric materials in enhancing the performance of conventional p–n junction PSCs, and further research could lead to the development of more efficient and stable PSCs.

Data availability

All data supporting the findings of this study are available within the main text and the ESI.† All relevant data are available from the corresponding authors upon reasonable request.

Conflicts of interest

The authors declare no conflicts of interest.

Acknowledgements

This work was supported by Australia's Economic Accelerator Seed Grants (AE230100350) and partially funded by the Australian Research Council (LP200200979). This work was also supported by the Korea Institute of Energy Technology Evaluation and Planning (KETEP) and the Ministry of Trade, Industry & Energy (MOTIE) of the Republic of Korea (No. RS-2024-00437030). J. S. Y. acknowledges the Royal Society research grant (RGS/R1/221369) and the support from the National Research Foundation of Korea (NRF) grant funded by the Korean government (MEST) (No. RS-2024-00333809 and No. RS-2023-00257494). Additional support was provided by the National Research Foundation of Korea (NRF) grant funded by the Korean government (MSIT) (No. RS-2023-00208467), and by the Korea Institute of Energy Technology Evaluation and Planning (KETEP) and the Ministry of Trade, Industry & Energy (MOTIE) of the Republic of Korea (No. 20214000000680).

References

1 J. Park, J. Kim, H.-S. Yun, M. J. Paik, E. Noh, H. J. Mun, M. G. Kim, T. J. Shin and S. Il Seok, *Nature*, 2023, **616**, 724–730.
2 S. Liu, J. Li, W. Xiao, R. Chen, Z. Sun, Y. Zhang, X. Lei, S. Hu, M. Kober-Czerny, J. Wang, F. Ren, Q. Zhou, H. Raza, Y. Gao, Y. Ji, S. Li, H. Li, L. Qiu, W. Huang, Y. Zhao, B. Xu, Z. Liu, H. J. Snaith, N.-G. Park and W. Chen, *Nature*, 2024, **632**, 536–542.
3 Z. Huang, Y. Bai, X. Huang, J. Li, Y. Wu, Y. Chen, K. Li, X. Niu, N. Li, G. Liu, Y. Zhang, H. Zai, Q. Chen, T. Lei, L. Wang and H. Zhou, *Nature*, 2023, **623**, 531–537.
4 C.-S. Jiang, M. Yang, Y. Zhou, B. To, S. U. Nanayakkara, J. M. Luther, W. Zhou, J. J. Berry, J. van de Lagemaat, N. P. Padture, K. Zhu and M. M. Al-Jassim, *Nat. Commun.*, 2015, **6**, 8397.
5 J. H. Heo, S. H. Im, J. H. Noh, T. N. Mandal, C.-S. Lim, J. A. Chang, Y. H. Lee, H. Kim, A. Sarkar, Md. K. Nazeeruddin, M. Grätzel and S. Il Seok, *Nat. Photonics*, 2013, **7**, 486–491.
6 P. Ru, E. Bi, Y. Zhang, Y. Wang, W. Kong, Y. Sha, W. Tang, P. Zhang, Y. Wu, W. Chen, X. Yang, H. Chen and L. Han, *Adv. Energy Mater.*, 2020, **10**, 1903487.
7 E. Edri, S. Kirmayer, S. Mukhopadhyay, K. Gartsman, G. Hodes and D. Cahen, *Nat. Commun.*, 2014, **5**, 3461.
8 R. Chen, J. Wang, Z. Liu, F. Ren, S. Liu, J. Zhou, H. Wang, X. Meng, Z. Zhang, X. Guan, W. Liang, P. A. Troshin, Y. Qi, L. Han and W. Chen, *Nat. Energy*, 2023, **8**, 839–849.
9 S. Tan, T. Huang, I. Yavuz, R. Wang, T. W. Yoon, M. Xu, Q. Xing, K. Park, D.-K. Lee, C.-H. Chen, R. Zheng, T. Yoon, Y. Zhao, H.-C. Wang, D. Meng, J. Xue, Y. J. Song, X. Pan, N.-G. Park, J.-W. Lee and Y. Yang, *Nature*, 2022, **605**, 268–273.
10 S. Zhang, F. Ye, X. Wang, R. Chen, H. Zhang, L. Zhan, X. Jiang, Y. Li, X. Ji, S. Liu, M. Yu, F. Yu, Y. Zhang, R. Wu, Z. Liu, Z. Ning, D. Neher, L. Han, Y. Lin, H. Tian, W. Chen, M. Stolterfoht, L. Zhang, W.-H. Zhu and Y. Wu, *Science*, 2023, **380**, 404–409.
11 S. R. Basu, L. W. Martin, Y. H. Chu, M. Gajek, R. Ramesh, R. C. Rai, X. Xu and J. L. Musfeldt, *Appl. Phys. Lett.*, 2008, **92**, 091905.
12 A. Bhatnagar, A. Roy Chaudhuri, Y. Heon Kim, D. Hesse and M. Alexe, *Nat. Commun.*, 2013, **4**, 2835.
13 H. Matsuo, Y. Noguchi and M. Miyayama, *Nat. Commun.*, 2017, **8**, 207.
14 S. Y. Yang, J. Seidel, S. J. Byrnes, P. Shafer, C.-H. Yang, M. D. Rossell, P. Yu, Y.-H. Chu, J. F. Scott, J. W. Ager, L. W. Martin and R. Ramesh, *Nat. Nanotechnol.*, 2010, **5**, 143–147.
15 Y. Wu, B. Chang, L. Wang, H. Li, L. Pan, Z. Liu and L. Yin, *Adv. Mater.*, 2023, **35**, 2300174.
16 B. Han, Y. Wang, C. Liu, K. Sun, M. Yang, L. Xie, S. Yang, Y. Meng, S. Lin, P. Xu, J. Li, Q. Qiu and Z. Ge, *Angew. Chem., Int. Ed.*, 2023, **62**, e202217526.
17 S. Heo, D. Y. Lee, D. Lee, Y. Lee, K. Kim, H.-S. Yun, M. J. Paik, T. J. Shin, H. S. Oh, T. Shin, J. Kim, S. H. Kim, S. Il Seok and M. Nazeeruddin, *Adv. Energy Mater.*, 2022, **12**, 2200181.
18 X. Zhao, T. Liu and Y.-L. Loo, *Adv. Mater.*, 2022, **34**, 2105849.
19 H. Kim, S.-U. Lee, D. Y. Lee, M. J. Paik, H. Na, J. Lee and S. Il Seok, *Adv. Energy Mater.*, 2019, **9**, 1902740.
20 Q. Jiang, Y. Zhao, X. Zhang, X. Yang, Y. Chen, Z. Chu, Q. Ye, X. Li, Z. Yin and J. You, *Nat. Photonics*, 2019, **13**, 460–466.
21 G. Wu, R. Liang, M. Ge, G. Sun, Y. Zhang and G. Xing, *Adv. Mater.*, 2022, **34**, 2105635.

22 X. Chang, R. Azmi, T. Yang, N. Wu, S. Y. Jeong, H. Xi, D. Satrio Utomo, B. Vishal, F. H. Isikgor, H. Faber, Z. Ling, M. He, M. Marengo, P. Dally, A. Prasetio, Y.-Y. Yang, C. Xiao, H. Y. Woo, K. Zhao, M. Heeney, S. De Wolf, L. Tsetseris and T. D. Anthopoulos, *Nat. Commun.*, 2025, **16**, 1042.

23 Y. Yan, R. Wang, Q. Dong, Y. Yin, L. Zhang, Z. Su, C. Wang, J. Feng, M. Wang, J. Liu, H. Ma, Y. Feng, W. Shang, Z. Wang, M. Pei, Y. Wang, S. Jin, J. Bian, X. Gao, S. Liu and Y. Shi, *Energy Environ. Sci.*, 2022, **15**, 5168–5180.

24 Y. Lin, Y. Bai, Y. Fang, Z. Chen, S. Yang, X. Zheng, S. Tang, Y. Liu, J. Zhao and J. Huang, *J. Phys. Chem. Lett.*, 2018, **9**, 654–658.

25 S. Gharibzadeh, B. Abdollahi Nejand, M. Jakoby, T. Abzieher, D. Hauschild, S. Moghadamzadeh, J. A. Schwenzer, P. Brenner, R. Schmager, A. A. Haghighirad, L. Weinhardt, U. Lemmer, B. S. Richards, I. A. Howard and U. W. Paetzold, *Adv. Energy Mater.*, 2019, **9**, 1803699.

26 Y.-W. Jang, S. Lee, K. M. Yeom, K. Jeong, K. Choi, M. Choi and J. H. Noh, *Nat. Energy*, 2021, **6**, 63–71.

27 C. Wang, J. Gu, J. Li, J. Cai, L. Li, J. Yao, Z. Lu, X. Wang and G. Zou, *Natl. Sci. Rev.*, 2023, **10**, nwad061.

28 Q. Zhang, A. Solanki, K. Parida, D. Giovanni, M. Li, T. L. C. Jansen, M. S. Pshenichnikov and T. C. Sum, *ACS Appl. Mater. Interfaces*, 2019, **11**, 13523–13532.

29 K. Wang, C. Wu, Y. Jiang, D. Yang, K. Wang and S. Priya, *Sci. Adv.*, 2024, **5**, eaau3241.

30 E. Choi, Y. Zhang, A. M. Soufiani, M. Lee, R. F. Webster, M. E. Pollard, P. J. Reece, W. Lee, J. Seidel, J. Lim, J.-H. Yun and J. S. Yun, *npj 2D Mater. Appl.*, 2022, **6**, 43.

31 C. Ortiz-Cervantes, P. Carmona-Monroy and D. Solis-Ibarra, *ChemSusChem*, 2019, **12**, 1560–1575.

32 C. Liu, Y. Yang, H. Chen, I. Spanopoulos, A. S. R. Bati, I. W. Gilley, J. Chen, A. Maxwell, B. Vishal, R. P. Reynolds, T. E. Wiggins, Z. Wang, C. Huang, J. Fletcher, Y. Liu, L. X. Chen, S. De Wolf, B. Chen, D. Zheng, T. J. Marks, A. Facchetti, E. H. Sargent and M. G. Kanatzidis, *Nature*, 2024, **633**, 359–364.

33 S. Chen, X. Xiao, B. Chen, L. L. Kelly, J. Zhao, Y. Lin, M. F. Toney and J. Huang, *Sci. Adv.*, 2024, **7**, eabb2412.

34 J. H. Heo, F. Zhang, C. Xiao, S. J. Heo, J. K. Park, J. J. Berry, K. Zhu and S. H. Im, *Joule*, 2021, **5**, 481–494.

35 J. Zhang, X. Zhu, M. Wang and B. Hu, *Nat. Commun.*, 2020, **11**, 2618.

36 S. Sadewasser and T. Glatzel, *Kelvin Probe Force Microscopy: From Single Charge Detection to Device Characterization*, Springer, 2018, vol. 65.

37 Y. Liu, D. Kim, A. V. Ievlev, S. V. Kalinin, M. Ahmadi and O. S. Ovchinnikova, *Adv. Funct. Mater.*, 2021, **31**, 2102793.

38 Y. S. Kim, D. H. Kim, J. D. Kim, Y. J. Chang, T. W. Noh, J. H. Kong, K. Char, Y. D. Park, S. D. Bu, J.-G. Yoon and J.-S. Chung, *Appl. Phys. Lett.*, 2005, **86**, 102907.

39 J. M. Frost, K. T. Butler, F. Brivio, C. H. Hendon, M. van Schilfgaarde and A. Walsh, *Nano Lett.*, 2014, **14**, 2584–2590.

40 D. A. Egger, A. M. Rappe and L. Kronik, *Acc. Chem. Res.*, 2016, **49**, 573–581.

41 Y. Kutes, L. Ye, Y. Zhou, S. Pang, B. D. Huey and N. P. Padture, *J. Phys. Chem. Lett.*, 2014, **5**, 3335–3339.

42 D. Kim, J. S. Yun, P. Sharma, D. S. Lee, J. Kim, A. M. Soufiani, S. Huang, M. A. Green, A. W. Y. Ho-Baillie and J. Seidel, *Nat. Commun.*, 2019, **10**, 444.

43 P. Sharma, F.-X. Xiang, D.-F. Shao, D. Zhang, E. Y. Tsymbal, A. R. Hamilton and J. Seidel, *Sci. Adv.*, 2023, **5**, eaax5080.

44 T.-T. Sha, Y.-A. Xiong, Q. Pan, X.-G. Chen, X.-J. Song, J. Yao, S.-R. Miao, Z.-Y. Jing, Z.-J. Feng, Y.-M. You and R.-G. Xiong, *Adv. Mater.*, 2019, **31**, 1901843.

45 L. Li, X. Liu, Y. Li, Z. Xu, Z. Wu, S. Han, K. Tao, M. Hong, J. Luo and Z. Sun, *J. Am. Chem. Soc.*, 2019, **141**, 2623–2629.

46 Z. Wu, C. Ji, L. Li, J. Kong, Z. Sun, S. Zhao, S. Wang, M. Hong and J. Luo, *Angew. Chem., Int. Ed.*, 2018, **57**, 8140–8143.

47 D. Kim, A. V. Ievlev, O. S. Ovchinnikova, S. V. Kalinin and M. Ahmadi, *J. Mater. Chem. A*, 2022, **10**, 10120–10131.

48 H. Tsai, R. Asadpour, J.-C. Blancon, C. C. Stoumpos, O. Durand, J. W. Strzalka, B. Chen, R. Verduzco, P. M. Ajayan, S. Tretiak, J. Even, M. A. Alam, M. G. Kanatzidis, W. Nie and A. D. Mohite, *Science*, 2018, **360**, 67–70.

49 H. Li, F. Li, Z. Shen, S.-T. Han, J. Chen, C. Dong, C. Chen, Y. Zhou and M. Wang, *Nano Today*, 2021, **37**, 101062.

50 X. Wu, L. Z. Tan, X. Shen, T. Hu, K. Miyata, M. T. Trinh, R. Li, R. Coffee, S. Liu, D. A. Egger, I. Makasyuk, Q. Zheng, A. Fry, J. S. Robinson, M. D. Smith, B. Guzelturk, H. I. Karunadasa, X. Wang, X. Zhu, L. Kronik, A. M. Rappe and A. M. Lindenberg, *Sci. Adv.*, 2024, **3**, e1602388.

51 D. Zhang, P. Schoenherr, P. Sharma and J. Seidel, *Nat. Rev. Mater.*, 2023, **8**, 25–40.

52 G. Xia, B. Huang, Y. Zhang, X. Zhao, C. Wang, C. Jia, J. Zhao, W. Chen and J. Li, *Adv. Mater.*, 2019, **31**, 1902870.

53 P. Wang, J. Zhao, L. Wei, Q. Zhu, S. Xie, J. Liu, X. Meng and J. Li, *Nanoscale*, 2017, **9**, 3806–3817.

54 Q. N. Chen, Y. Ou, F. Ma and J. Li, *Appl. Phys. Lett.*, 2014, **104**, 242907.

55 C. Cazorla, M. Stengel, J. Íñiguez and R. Rurali, *npj Comput. Mater.*, 2023, **9**, 97.

56 Z. Liu, C. Menéndez, J. Shenoy, J. N. Hart, C. C. Sorrell and C. Cazorla, *Nano Energy*, 2020, **72**, 104732.

57 D. Liu, Y. Wu, M. R. Samatov, A. S. Vasenko, E. V. Chulkov and O. V. Prezhdo, *Chem. Mater.*, 2024, **36**, 2898–2906.

58 J. S. Yun, J. Seidel, J. Kim, A. M. Soufiani, S. Huang, J. Lau, N. J. Jeon, S. Il Seok, M. A. Green and A. Ho-Baillie, *Adv. Energy Mater.*, 2016, **6**, 1600330.

59 J. S. Yun, A. Ho-Baillie, S. Huang, S. H. Woo, Y. Heo, J. Seidel, F. Huang, Y.-B. Cheng and M. A. Green, *J. Phys. Chem. Lett.*, 2015, **6**, 875–880.